REPORT DOCUMENTATION PAGE

Form Approved OMB NO. 0704-0188

The public reporting burden for this collection of information is estimated to average 1 hour per response, including the time for reviewing instructions, searching existing data sources, gathering and maintaining the data needed, and completing and reviewing the collection of information. Send comments regarding this burden estimate or any other aspect of this collection of information, including suggesstions for reducing this burden, to Washington Headquarters Services, Directorate for Information Operations and Reports, 1215 Jefferson Davis Highway, Suite 1204, Arlington VA, 22202-4302. Respondents should be aware that notwithstanding any other provision of law, no person shall be subject to any oenalty for failing to comply with a collection of information if it does not display a currently valid OMB control number.
PLEASE DO NOT RETURN YOUR FORM TO THE ABOVE ADDRESS.

1. REPORT DATE (DD-MM-YYYY)	2. REPORT TYPE	3. DATES COVERED (From - To)
	New Reprint	-

4. TITLE AND SUBTITLE	5a. CONTRACT NUMBER
InAs/GaSb Broken-Gap Heterostructure Laser for Terahertz Spectroscopic Sensing Application	
	5b. GRANT NUMBER
	W911NF-04-D-0003
	5c. PROGRAM ELEMENT NUMBER
	611102

6. AUTHORS	5d. PROJECT NUMBER
Weidong Zhang, Dwight Woolard	
	5e. TASK NUMBER
	5f. WORK UNIT NUMBER

7. PERFORMING ORGANIZATION NAMES AND ADDRESSES	8. PERFORMING ORGANIZATION REPORT NUMBER
North Carolina State University Research Administration 2701 Sullivan Drive, Suite 240 Raleigh, NC 27695 -7514	

9. SPONSORING/MONITORING AGENCY NAME(S) AND ADDRESS(ES)	10. SPONSOR/MONITOR'S ACRONYM(S)
U.S. Army Research Office P.O. Box 12211 Research Triangle Park, NC 27709-2211	ARO
	11. SPONSOR/MONITOR'S REPORT NUMBER(S)
	52918-EL-SR.5

12. DISTRIBUTION AVAILIBILITY STATEMENT

Approved for public release; distribution is unlimited.

13. SUPPLEMENTARY NOTES

The views, opinions and/or findings contained in this report are those of the author(s) and should not contrued as an official Department of the Army position, policy or decision, unless so designated by other documentation.

14. ABSTRACT

A completely new type of solid-state laser device
is presented that offers the potential for achieving significantly
increased levels of terahertz (THz) frequency output power at
relatively high operating temperatures. Specifically, a doublebarrier
GaSb/InAs/GaSb heterostructure device concept is introduced

15. SUBJECT TERMS

InAs/GaSb, heterostructure, conduction band,heavy hole, interband, lasing, nonradiative transitions.

16. SECURITY CLASSIFICATION OF:			17. LIMITATION OF ABSTRACT	15. NUMBER OF PAGES	19a. NAME OF RESPONSIBLE PERSON
a. REPORT	b. ABSTRACT	c. THIS PAGE			Dwight Woolard
UU	UU	UU	UU		19b. TELEPHONE NUMBER
					919-549-4297

Standard Form 298 (Rev 8/98)
Prescribed by ANSI Std. Z39.18

Report Title

InAs/GaSb Broken-Gap Heterostructure Laser for Terahertz Spectroscopic Sensing Application

ABSTRACT

A completely new type of solid-state laser device is presented that offers the potential for achieving significantly increased levels of terahertz (THz) frequency output power at relatively high operating temperatures. Specifically, a doublebarrier GaSb/InAs/GaSb heterostructure device concept is introduced that simultaneously leverages resonant electron injection and interband tunneling electron depletion to realize electron population inversion, while at the same time mitigating the scattering effects that degrade the lasing process. Here, the main innovations are the ability to spatially separate the upper and lower electron populations using the quantum confinement of the double-barrier conduction band well and the valence-band well (i.e., of the second barrier), respectively, and the depopulation of the valence-band well by heavy hole interband tunneling. A theoretical analysis of the radiative and nonradiative transition rates based upon a multiband Kane model formalism is used to confirm the large available optical gain and to estimate the lasing output power at very long wavelengths. Therefore, this work establishes the initial foundation for a solid-state THz laser that can provide significant levels of output power below 1 THz. Furthermore, the inherently high spectral purity and natural tunability offered by this novel laser technology will be instrumental in future spectroscopic analysis of nanoscale biological and/or organic systems that are well known to possess unique spectral signatures at very long wavelengths.

Continuation for Block 13

ARO Report Number   52918.5-EL-SR
InAs/GaSb Broken-Gap Heterostructure Laser fo   ...

Block 13: Supplementary Note

InAs/GaSb Broken-Gap Heterostructure Laser for Terahertz Spectroscopic Sensing Application

Weidong Zhang, *Member, IEEE*, and Dwight L. Woolard, *Fellow, IEEE*

Abstract—A completely new type of solid-state laser device is presented that offers the potential for achieving significantly increased levels of terahertz (THz) frequency output power at relatively high operating temperatures. Specifically, a double-barrier GaSb/InAs/GaSb heterostructure device concept is introduced that simultaneously leverages resonant electron injection and interband tunneling electron depletion to realize electron-population inversion, while at the same time mitigating the scattering effects that degrade the lasing process. Here, the main innovations are the ability to spatially separate the upper and lower electron populations using the quantum confinement of the double-barrier conduction band well and the valence-band (VB) well (i.e., of the second barrier), respectively, and the depopulation of the VB well by heavy hole interband tunneling. A theoretical analysis of the radiative and nonradiative transition rates based upon a multiband Kane model formalism is used to confirm the large available optical gain and to estimate the lasing output power at very long wavelengths. Therefore, this study establishes the initial foundation for a solid-state THz laser that can provide significant levels of output power below 1 THz. Furthermore, the inherently high spectral purity and natural tunability offered by this novel laser technology will be instrumental in future spectroscopic analysis of nanoscale biological and/or organic systems that are well known to possess unique spectral signatures at very long wavelengths.

Index Terms—Conduction band, heavy hole, heterostructure, InAs/GaSb, interband, lasing, nonradiative transitions.

I. INTRODUCTION

THE key technological property of broken-gap InAs/GaSb heterostructure from the 6.1 Å family is that the valence-band (VB) bottom of GaSb is 0.15 eV above the conduction-band (CB) bottom of InAs [1]. Hence, within the adjacent InAs conduction-band (CB) well and the GaSb heavy-hole (HH) VB well systems, the individual electron and hole energy-levels may be positioned close enough to allow for very long wavelength recombination while the same time the overlaps of individually quantum confined wave functions are small. It is useful to note that this set of quasi-bound systems allows for a finite in-terband (i.e., conduction to valence) recombination process to exist and that the small overlap will significant reduce important scattering effects (e.g., phonon and Auger) that typical degrade lasing. Furthermore, as will be shown, it is possible to utilize interband tunneling to rapidly drain the electrons from the VB well and to achieve significant population inversions and optical gain. The fact that alloying with aluminum or indium may modify band-edge alignments adds additional flexibility for design of the device's operational frequency and lasing performance. For these general reasons, the InAs/GaSb heterostructure is of great interest for applications in long wavelength light emitting devices and detectors. To date, these investigations have been limited to the study of radiation sources in the infrared regime, with some examples being: Type-II intersubband lasers as described in [2] and [3]; a Type-II cascade lasing device as given in [4]; and, a W-shape Type-II midinfrared laser discussed in [5]. This paper extends a more recent development of a unipolar double-barrier staggered AlGaSb/InAs/AlGaSb interband tunneling diode (I-RTD) for midinfrared lasing [6], [7]. The basic concept is to utilize the electron injection produced by the resonant tunneling through the CB-well structure (i.e., formed by the double AlGaSb barriers and InAs well) as the source of the lasing, and the HH population generated within the VB well (i.e., formed by the right AlAsSb barrier) by interband Zener tunneling as the recombination sink. The basic utility of the broken-gap I-RTD lasing process for realizing far-infrared to THz radiation was recently summarized by our group in [8], and the goal of this study is to assess a specific InAs/GaSb broken-gap heterostructure laser design that has been tailored for THz-frequency operation.

The basic energy-band structure of the broken-gap I-RTD laser device considered in this study is illustrated in Fig. 1(a). As illustrated in Fig. 1(b), the left-hand side of the device will be implemented with a heavily doped n^+ InAs layer on the left which forms the diode emitter and a combined undoped (spacer) and n^+ InAs layer on the right-hand side, which forms the diode collector. Electrons will then be injected into the higher energy level E_2 that is quasi-confined in the InAs CB-well region when the structure is subjected to a forward-biasing external voltage, and this will be accompanied by a depopulation of electrons from the lower energy level E_1 that is quasi-confined in the right GaSb VB well region by HH interband tunneling of electrons into the undoped spacer region.

The carrier inversion for the two-energy system defined in Fig. 2 may be estimated using the equation [9], $\Delta N = \eta_i J(\tau_{21} - \tau_1)/e$, where η_i is the quantum efficiency, J is the CB resonant current, τ_{21} is the relaxation time constant of energy level 2, and τ_1 is the time constant for removal of

W. Zhang is with the Department of Electrical and Computer Engineering, North Carolina State University, Raleigh, NC 27695 USA (e-mail: wzhang5@ncsu.edu).

D. L. Woolard is with the U.S. Army Research Laboratory, U.S. Army Research Office, Research Triangle Park, NC 27709 USA.
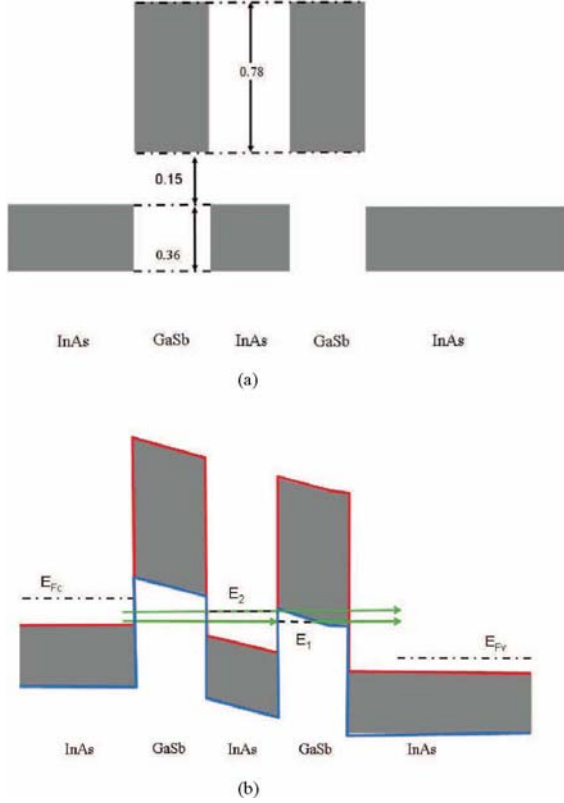
Fig. 1. Broken-gap device structure for THz lasing. (a) Without bias. (b) Under bias.

Fig. 2. Two-energy level model for electron's injection and removal. The energy levels in emitter's and collector's reservoir are not sketched.

carrier from energy level 1. The relaxation time is written as $1/\tau_{21} = 1/\tau_{\rm sp} + 1/\tau_{\rm ap} + 1/\tau_{\rm op} + 1/\tau_{\rm Aug}$, where $\tau_{\rm sp}$ is the spontaneous recombination time constant, $\tau_{\rm ap}$ is the acoustic phonon scattering time constant, $\tau_{\rm op}$ is the optical phonon scattering time constant, and $\tau_{\rm Aug}$ is the Auger recombination time constant. The key to establishing a useful population inversion is that charging rate $(1/\tau_1)$ of the E_1 by HH tunneling can be made much faster than the net relaxation rate $(1/\tau_{21})$. This fact will be substantiated by the modeling and simulation work that is presented shortly.

Section II-A, II-B, and II-C will present physical models that are accurate for addressing the most important issues related to the broken-gap I-RTD laser device; namely, the multiband transport models, transition probabilities, and the self-consistent charging effects which can be combined together to estimate all the flux processes and the overall depopulation dynamics. Section II-D provides an assessment of a specific broken-gap I-RTD laser design that targets THz frequency operation. The main conclusions of this study are: 1) CB energy level E_2 and heavy hole level E_1 are amenable to the production of long wave radiation; 2) the HH interband tunneling is fast enough for electron depopulation; 3) nonradiative process rates that degrade performance can be suppressed; and 4) substantial optical gain can be obtained.

II. MODELING AND SIMULATION RESULTS

The study of transport dynamics in this broken-gap and narrow-band structure must be based upon a six-band Kane
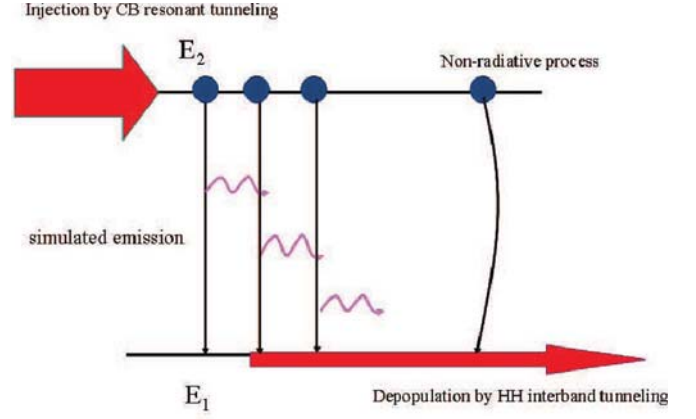
model formulism of the type previously developed in [10] and [11]. This model allows for the treatment of the strong multiband coupling effects that originate from the narrow bandgaps and band edge misalignments. A complete description of the CB electron motion requires a set of envelope functions $\Psi_\sigma^{\rm (CB)} = \left\{ a_{c\sigma}^{\rm (CB)}, a_{l\sigma}^{\rm (CB)}, a_{h\sigma}^{\rm (CB)} \right\}$, where $a_{c\sigma}^{\rm (CB)}$ is the conduction band (CB), $a_{l\sigma}^{\rm (CB)}$ is the light-hole (LH) band, and $a_{h\sigma}^{\rm (CB)}$ is the heavy-hole (HH) band components. Here, the subscript σ denotes the two possible spin state, i.e., $\pm$. Similarly, the HH electron dynamics in the VB requires another set of envelope functions denoted as $\Psi_\sigma^{\rm (HH)} = \left\{ a_{c\sigma}^{\rm (HH)}, a_{l\sigma}^{\rm (HH)}, a_{h\sigma}^{\rm (HH)} \right\}$.

The net CB transmission of electrons from emitter to collector arises through contributions from two distinct channels. The first channel is from resonant tunneling through the CB-well that is defined by the GaSb/InAs/GaSb double-barrier structure. This electron flux component is illustrated by the upper horizontal arrow in Fig. 1(b). The second channel is from interband tunneling of electrons that are allowed to leave the HH level within the right VB well and that enter into the spacer-collector region. This electron flux component is illustrated by the lower horizontal arrow on the right side of HH-state E_1 as also shown in Fig. 1(b). Here, it is valuable to note that these VB well electrons can be sourced from interband tunneling from the emitter [i.e., see lower horizontal arrow on the left-hand side of HH-state E_1 in Fig. 1(b)] and from electron recombination that occurs from E_2 to E_1 transitions. However, as will be demonstrated later, the contribution from interband tunneling from the emitter is insignificant when forward biasing is applied. This means that HHs will accumulate in the right VB well, and then collectively serve as a localized recombination center for CB electrons that are injected into the CB-well. This recombination will arise from both radiative or nonradiative processes.

A. Transport Equations

The Kane model from [10] and [11] is useful for describing the wavefunctions through the various regions of the broken-gap structure illustrated in Fig. 1. The CB electrons in the InAs

regions are governed by the coupled differential equations

$$\sqrt{\frac{2}{3}}P\left(\frac{d}{dz} \pm \frac{1}{2}k_t\right)a_{l\sigma}^{(CB)} = -i\left[(U - E - eV_a)a_{c\sigma}^{(CB)}\right.$$

$$\left. + \frac{P^2 k_t^2}{2(E + eV_a - U + E_{gw})}a_{c\sigma}^{(CB)}\right] \tag{1}$$

$$\sqrt{\frac{2}{3}}P\left(\frac{d}{dz} \mp \frac{1}{2}k_t\right)a_{c\sigma}^{(CB)} = i(E + eV_a + E_{gw} - U)a_{l\sigma}^{(CB)} \tag{2}$$

where E_{gw} is the band gap of InAs, V_a is the bias voltage, $k_t = \sqrt{k_x^2 + k_y^2}$ is the in-plane momentum, e is the charge of electron, and P is Kane interband parameters. Here, E is referenced to the CB bottom in the emitter. The coupled differential equation system for CB electrons in the GaSb regions is

$$\sqrt{\frac{2}{3}}P\left(\frac{d}{dz} \pm \frac{1}{2}k_t\right)a_{l\sigma}^{(CB)} = -i\left[(U + \Delta_c - E - eV_a)a_{c\sigma}^{(CB)}\right.$$

$$\left. + \frac{P^2 k_t^2}{2(E + eV_a - U + E_{gw})}a_{c\sigma}^{(CB)}\right] \tag{3}$$

$$\sqrt{\frac{2}{3}}P\left(\frac{d}{dz} \mp \frac{1}{2}k_t\right)a_{c\sigma}^{(CB)} = i(E + eV_a + E_{gb} - U - \Delta_c)a_{l\sigma}^{(CB)} \tag{4}$$

where E_{gb} is the band gap of GaSb; and Δ_c is the conduction band offset. Due to the fact that the LH and HH contributions to the CB transport should be small, the Kane model directly reveals that the HH component may be estimated from the linear equation

$$a_{h\sigma}^{(CB)} = \frac{\mp\frac{1}{\sqrt{2}}Pk_t}{E + eV_a - U + E_{gw}}a_{c\sigma}^{(CB)}. \tag{5}$$

For resonant transmission in the CB, the wavefunction in the collector on the right (R) is only an outgoing wave, which leads to the relations

$$a_{Rc\sigma}^{(CB)} = t_{Rc}\frac{\exp{(ik_{Rz}z)}}{\sqrt{N_R}} \tag{6}$$

$$a_{Rl\sigma}^{(CB)} = \sqrt{\frac{2}{3}}P\left(k_{Rz} \pm i\frac{k_t}{2}\right)\frac{t_{Rc}\exp{(ik_{Rz}z)}}{(E + eV_a + E_{gw})\sqrt{N_R}} \tag{7}$$

where t_{Rc} is the transmission coefficient, N_R is the normalization constant, and the outgoing wave vector k_R can be obtained from the dispersion relation of energy [10]. The wavefunction in the emitter on the left (L) must be the sum of incoming and reflected waves, which leads to

$$a_{Lc\sigma}^{(CB)} = \frac{1}{\sqrt{N_L}}\left[\exp{(ik_{Lz}z)} + r_L\exp{(-ik_{Lz}z)}\right] \tag{8}$$

$$a_{Ll\sigma}^{(CB)} = \frac{1}{(E + E_{gw})\sqrt{N_L}}\sqrt{\frac{2}{3}}P\left[\left(k_{Lz} \pm i\frac{k_t}{2}\right)\exp{(ik_{Lz}z)}\right.$$

$$\left. + \left(-k_{Lz} \pm i\frac{k_t}{2}\right)r_L\exp{(-ik_{Lz}z)}\right]. \tag{9}$$

Here, r_L is the reflection coefficient and N_L is the normalization constant [10]. In both (8) and (9), the first term represents the incident wave beginning from the emitter contact while the second term accounts for the reflection by potential barriers. also, k_{Lz} is the wave vector of propagation. Therefore, the system defined by (1), (2), (8), and (9) leads to a dispersion law of

$$E(E + E_{gw}) = \frac{\hbar^2 E_{gw}}{2m_w}\left(k_{Lz}^2 + k_t^2\right) \tag{10}$$

where $m_w = 0.023m_0$ is the electron's effective mass in InAs layers. Furthermore, if the resonant energy level in the CB-well is referenced to the VB edge at the collector contact (this will be needed later) then it can be expressed as

$$E_2 = E + E_{gw} + eV_a. \tag{11}$$

The interband tunneling can only through CB-LH-HH multi-band coupling effects, and it is possible to deduce that it will be dominated by the HH confined state within the right VB well (i.e., HH state will be closet to the VB edge). Hence, it is acceptable to assume that $a_l^{(HH)}$ and $a_c^{(HH)}$ are an order of magnitude less than $a_h^{(HH)}$, which leads to the following systems of differential equations describing the wavefunctions in the right VB well

$$\sqrt{\frac{2}{3}}P\left(\frac{d}{dz} \mp \frac{1}{2}k_t\right)a_{l\sigma}^{(HH)}$$

$$= -(E_{gb} + U + \Delta_v - E_h)a_{c\sigma}^{(HH)} \pm \frac{1}{\sqrt{2}}Pk_t a_{h\sigma}^{(HH)} \tag{12}$$

$$\sqrt{\frac{2}{3}}P\left(\frac{d}{dz} \pm \frac{1}{2}k_t\right)a_{c\sigma}^{(HH)} = (E_{gb} + U + \Delta_v - E_h)a_{l\sigma}^{(HH)} \tag{13}$$

$$\frac{\hbar^2}{2m_h}\frac{d^2}{dz^2}a_{h\sigma}^{(HH)} - [E_h - U(z) - \Delta_v]a_{h\sigma}^{(HH)} = 0 \tag{14}$$

where Δ_v is the VB offset, $m_h = 0.40m_0$ is the effective mass of heavy hole, and E_h is the quasi-bound heavy-hole level. All the energies are referenced to the CB bottom at the collector contact. In the InAs regions, the differential equations are obtained by replacing the band gap E_{gb} with E_{gw}, and letting $\Delta_v = 0$. The localized heavy-hole wavefunctions at the boundaries of the device contacts can be written as

$$a_{h\sigma}^{(HH)} = b_{hL}\exp{(\kappa_{Lh}z)} \tag{15}$$

$$a_{h\sigma}^{(HH)} = b_{hR}\exp{(-\kappa_{Rh}z)} \tag{16}$$

where $\kappa_{Lh} = \sqrt{2m_h(E_h - eV_a)}/\hbar$ and $\kappa_{Rh} = \sqrt{2m_h E_h}/\hbar$ at the emitter and collector contacts, respectively. The quasi-bound E_h can be estimated from (14). The solutions of $a_{c\sigma}^{(HH)}$ and $a_{l\sigma}^{(HH)}$ in the emitter region must be written as

$$a_{c\sigma}^{(HH)} = B_{cL\sigma}\exp{(ik_L z)} + b_{cL\sigma}\exp{(\kappa_{Lh}z)} \tag{17}$$

$$a_{l\sigma}^{(HH)} = B_{lL\sigma}\exp{(ik_L z)} + b_{lL\sigma}\exp{(\kappa_{Lh}z)} \tag{18}$$

where the propagating terms allows for the possibility of electrons from the emitter region to successfully enter into the HH level of the right VB well via interband tunneling. Of course,

these electrons contributes no radiation. The wave vector k_L is

$$k_L = \sqrt{\frac{3}{2P^2}\left[E_h - (E_{gw} + eV_a)\right](E_h - eV_a) - \frac{1}{4}k_t^2}. \quad (19)$$

Similarly, the solutions in the collector region are

$$a_{c\sigma}^{(\mathrm{HH})} = A_{cR\sigma}\exp(ik_R z) + b_{cR\sigma}\exp(-\kappa_{Rh}z) \quad (20)$$

$$a_{l\sigma}^{(\mathrm{HH})} = A_{lR\sigma}\exp(ik_R z) + b_{lR\sigma}\exp(-\kappa_{Rh}z) \quad (21)$$

where the propagating terms represent the possibility of electrons enter into collector via interband tunneling. The wave vector k_R is

$$k_R = \sqrt{\frac{3}{2P^2}E_h(E_h - E_{gw}) - \frac{1}{4}k_t^2}. \quad (22)$$

The rate of HH electron tunneling out of (and into) the VB well can be evaluated from

$$\frac{1}{\tau_1} = \frac{4P^2}{3\hbar}\left[\frac{k_R}{E_h}|A_{cR\pm}(k_t)|^2 - \frac{k_L}{E_h - eV_a}|B_{cL\pm}(k_t)|^2\right] \quad (23)$$

where k_R (k_L) is outgoing (incoming) wave vector for the HHs and $|A_{cR\pm}(k_t)|^2$ ($|B_{cL\pm}(k_t)|^2$) is the interband tunneling probability of the outgoing (incoming) HHs. Hence, (23) is the central result for determining the depopulation dynamics. The net variation of charge in the right VB well due to outgoing and incoming electron tunneling is now definable from

$$\frac{dQ}{dt} = e\int\frac{k_t\,dk_t}{2\pi}\frac{1}{\tau_1} \quad (24)$$

where the last equation represents a consistent detailed balance-type summation over all the available HH states. HH energy is defined from

$$E_1 = E_h - \frac{\hbar^2 k_t^2}{2m_h}. \quad (25)$$

One should note that the energy levels given in both (11) and (25) include the energy contributions from the quantum confinement (i.e., the z-direction) and from the in-plane direction. This is actually very important as this interband laser will derive radiation from many equivalent energy differences that arise from these nonlinear dispersion laws and this lead to increased optical gain and bandwidth as compared to an intraband laser.

B. Transition Processes

1) Optical Recombination: The matrix element for optical transition is $\langle f|\overrightarrow{\varepsilon}\cdot\mathbf{p}|i\rangle$ between initial state $|i\rangle$ and final state $|f\rangle$, where $\overrightarrow{\varepsilon}$ is the polarization direction of the emitted light and $\mathbf{p}$ is the momentum operator for the electron. The initial state is $|\Psi^{(\mathrm{CB})}\rangle = a_{c\sigma}^{(\mathrm{CB})}|S_\sigma\rangle + a_{l\sigma}^{(\mathrm{CB})}|\nu_{l\sigma}\rangle + a_{h\sigma}^{(\mathrm{CB})}|\nu_{h\sigma}\rangle$, the final state is $|\Psi^{(\mathrm{HH})}\rangle = a_{h\sigma}^{(\mathrm{HH})}|\nu_{h\sigma}\rangle$, where $S_\sigma\rangle$, $|\nu_{l\sigma}\rangle$, and $|\nu_{h\sigma}\rangle$ are the Bloch base functions

$$|S_\pm\rangle = \frac{1}{\sqrt{2}}[-i\exp(-i\phi)|S\uparrow\rangle \pm |S\downarrow\rangle] \quad (26)$$

$$|\nu_{l\pm}\rangle = \frac{1}{\sqrt{2}}\left\{\exp(-i\phi)\left[-i\sqrt{\frac{2}{3}}|Z\uparrow\rangle + i\frac{1}{\sqrt{6}}|(X+iY)\downarrow\rangle\right]\right.$$
$$\left.\pm\left[\sqrt{\frac{2}{3}}|Z\downarrow\rangle + \frac{1}{\sqrt{6}}|(X-iY)\uparrow\rangle\right]\right\} \quad (27)$$

$$\nu_{h\pm}\rangle = \frac{1}{\sqrt{2}}\left[\pm\exp(-2i\phi)\frac{1}{\sqrt{2}}|(X+iY)\uparrow\rangle\right.$$
$$\left. + \exp(i\phi)\frac{1}{\sqrt{2}}i|(X-iY)\downarrow\rangle\right] \quad (28)$$

where the phase angle is $\phi = \arctan(k_y/k_x)$. k_x and k_y are the projections of momentum in x and y directions. The key point to make here is that these multiband wavefunctions can be used to show that the emitted light will be circularly polarized (see examples in [12]) and the strength of the optical emission is strongly associated with the interband interaction parameter P. By using these same wavefunctions in the matrix element for optical transition leads to a time constant for the spontaneous transition rate of

$$\frac{1}{\tau_{\mathrm{sp}}} = \frac{4m_w e^2 P^2 n_r}{\hbar^4 c^3}$$

$$\times\int\frac{d\omega(\omega/k_{L0})|\left\langle a_h^{(\mathrm{HH})}|a_c^{(\mathrm{CB})}\right\rangle|^2 f_c(1 - f_v)}{\left[1 + \frac{2\hbar^2(k_{L0}^2 + k_t^2)}{m_w E_{gw}}\right]^{-\frac{1}{2}} + \frac{m_w}{m_h}} \quad (29)$$

where n_r is diffraction index, $\hbar\omega$ is photon energy, c is the speed of light, and k_{L0} is root of equation $E_2 - E_1 = \hbar\omega$. f_c is Fermi functions for the initial electron state (i.e., equal to that in the emitter); f_v is Fermi function for final hole state; $E_{Fc} = E_F + E_{gw} + eV_a$, the Fermi energy at the emitter, k_B is Boltzmann constant, and T is temperature. The major nonradiative processes include acoustic/optical scattering and Auger recombination and they will be considered in the following two sections.

2) Phonon Scattering: The initial states consist of CB electrons are undergoing resonant tunneling and therefore possess a momentum $\{k_x, k_y, k_{Lz}\}$, where k_x is the x-direction wave vector and k_y is the y-direction wave vector. Conversely, the final states are confined HHs and only possess in-plane momentum $\{k_{x'}, k_{y'}\}$ where $k_{x'}$ is the x-direction wave vector, and $k_{y'}$ is the y-direction wave vector. $\mathbf{q}$ is the wave vector of phonon with projected spatial components $\{q_x, q_y, q_z\}$. $q = |\mathbf{q}|$ is the magnitude of phonon wave vector. For phonon emission, the in-plane momentum satisfies $q_x = k_x - k_{x'}$ and $q_y = k_y - k_{y'}$. Hence, the magnitude is evaluated from $q = \sqrt{(k_x - k_{x'})^2 + (k_y - k_{y'})^2 + q_z^2}$. The acoustic and optical phonon scattering rates for a specified final state are written as [13]

$$\frac{1}{\tau_{\mathrm{ap}}} = \frac{D^2}{16\pi^3\hbar\rho s^2}\int d^3k\,dq_z|I(q)|^2(f_c - f_v)$$

$$\times\left\{\left[\exp\left(\frac{\hbar\omega_q}{k_B T}\right) - 1\right]^{-1} + 1\right\}\delta(E_2 - E_1 - \hbar\omega_q) \quad (30)$$

and

$$\frac{1}{\tau_{\mathrm{op}}} = \frac{e^2\omega_0}{4\pi^2}\left(\frac{1}{\varepsilon_\infty} - \frac{1}{\varepsilon_0}\right)\int d^3k\,dq_z\frac{|I(q)|^2}{q^2}(f_c - f_v)$$

$$\times\left\{\left[\exp\left(\frac{\hbar\omega_q}{k_B T}\right) - 1\right]^{-1} + 1\right\}\delta(E_2 - E_1 - \hbar\omega_q) \quad (31)$$

where D is deformation potential, $\hbar\omega_q$ is acoustic phonon energy, s is velocity of sound, ρ is the mass density in the semiconductor, $\hbar\omega_0$ is the optical phonon energy, ε_∞ is high-frequency dielectric constant, ε_0 is static dielectric constant. For the acoustic phonon, there is dispersion relationship $\omega_q = sq$. The matrix element is written as

$$I(q_z) = \int a_{h\sigma}^{(\mathrm{HH})*} \exp{(iq_z z)} a_{h\sigma}^{(\mathrm{CB})} dz \quad (32)$$

where the wavefunctions are calculated from multiband Kane models defined in Section II-A.

3) CHHH Auger Recombination: A CB electron may recombine without emitting radiation by releasing kinetic energy to a second HH in the proper amount, i.e., $E_2 - E_1$. In this so-called "CHHH" process, the CB electron (i.e., the "C" in "CHHH") initially has the energy $E_{e1'} = eV_a + E_{gw} + E(\mathbf{q}_{1'})$ and momentum $\mathbf{q}_{1'}$, in which $E(\mathbf{q}_{1'})$ is defined the same as in (10). The recombining HH (i.e., the first "H" in "CHHH") initially has the energy $E_{h1} = E_h - (\hbar^2 q_1^2/2m_h)$ and momentum $\mathbf{q}_1$. During the Auger process, the recombining HH will give up energy to a second HH (i.e., the second "H" in "CHHH") which initially has the energy $E_{h2'} = E_h - (\hbar^2 q_{2'}^2/2m_h)$ and momentum $\mathbf{q}_{2'}$. After the Auger process, the second hole (i.e., the third "H" in "CHHH") will have the energy $E_{h2} = E_h - (\hbar^2 q_2^2/2m_h)$ and momentum $\mathbf{q}_2$. The projected components of $\mathbf{q}_{1'}$ are labeled as $q_{1'x}$, $q_{1'y}$, and $q_{1'z}$. Similar notations are used for $\mathbf{q}_1$, $\mathbf{q}_2$, and $\mathbf{q}_{2'}$. The resulting transitions rate for CHHH Auger recombination can be estimated from [14]

$$\frac{1}{\tau_{\mathrm{Aug}}} = \frac{2m_w e^4}{\hbar^3 \varepsilon_r^2 \pi^2} \int dq_{1'x} dq_{1'y} dq_{2x} dq_{2y}$$

$$\left| \int dq_z \frac{\langle a_{c1'}^{(\mathrm{CB})}| \exp{(iq_z z_1)}|a_{h1}^{(\mathrm{HH})}\rangle \langle a_{h2'}^{(\mathrm{HH})}| \exp{(-iq_z z_2)}|a_{h2}^{(\mathrm{HH})}\rangle}{q_z^2 + (q_{1x} - q_{1'x})^2 + (q_{1y} - q_{1'y})^2} \right|^2$$

$$\frac{1}{q_{1'z0}} \left[\frac{\hbar^2 q_{1'z0}^2}{2m_w E_{gw}} + \frac{\hbar^2 (q_{1'x}^2 + q_{1'y}^2)}{2m_w E_{gw}} \right]^{1/2} f(E_{e1'}) [1 - f(E_{h1})]$$

$$[1 - f(E_{h2})][1 - f(E_{h2'})] \quad (33)$$

where ε_r is dielectric constant. $q_{1'z0}$ is found from the energy conservation relationship $E_{e1'} - E_{h1} = E_{h2'} - E_{h2}$. Here, the screening effect is not taken into account. Also, CCCH Auger recombination (i.e., where two electrons are involved) is ignored because the electron filling over the available CB states due to resonant emitter injection is much more prolific than the creation of the allowable HH's in the VB well due to interband tunneling. This means that the extent of electron filling over CB energies will be much greater than the extent HH creation over the VB well energies, and this will significantly reduce the opportunity for two-electron scattering (i.e., due to the lack of unfilled energy states within the small $E_2 - E_1$ window) as compared to two-HH scattering.

4) Optical Gain: Similar to (29), Fermi's Golden rule may be combined with the multiband models for electron and hole

dynamics to estimate the total optical gain as [7]

$$G = \frac{m_w e^2 P^2}{\hbar^4 c n_r \omega} \int_0^{k_{t\max}} dk_z \left(\sum_{\sigma = \pm} |\langle a_{h\sigma}^{(\mathrm{HH})}|a_{c\sigma}^{(\mathrm{CB})}\rangle|^2 \right)$$

$$\times \left\{ \left[1 + \frac{2\hbar^2 (k_{t0}^2 + k_z^2)}{m_w E_{gw}} \right]^{-\frac{1}{2}} + \frac{m_w}{m_h} \right\}^{-1} (f_c - f_v) \quad (34)$$

where k_{t0} need be evaluated from $E_2 - E_1 = \hbar\omega$, where E_2 is defined in (11) and E_1 is defined in (25).

C. Self-Consistent Calculation

The resulting potential profile for the active region of the device estimated from Poisson's equation where the major charging will arise from the accumulated sheet HH-charge density and leads to the relation

$$\rho_h = \frac{e k_{te}^2}{2\pi} \left| a_h^{(\mathrm{HH})} \right|^2 \quad (35)$$

where k_{te} is the maximum wave vector for HH states and can be derived from

$$E_h \mp \frac{1}{\sqrt{2}} P k_{te} \mathrm{Re} \left(\int_{-\infty}^{+\infty} a_h^{(\mathrm{HH})*} a_{c\pm}^{(\mathrm{HH})} dz \right)$$

$$- \frac{\hbar^2 k_{te}^2 (\gamma_1' + \gamma_2')}{2m_0} = E_{Fv} \quad (36)$$

where E_{Fv} is the Fermi energy level in collector. γ_1' and γ_2' are modified Luttinger parameters. While electron accumulation in the CB well will have some influence on the operation of the device (e.g., adjust the required terminal biasing), the primary driver in determining the overall carrier dynamics and associated transitions is the VB-well charging. Hence, to reduce the difficulty of the numerical simulations for achieving the first performance estimates of the laser device, the inclusion of the CB-well charging has been reserved for later investigations.

D. Simulation Results

Numerical simulation studies were performed to derive all the wavefunctions for a specific design of the structure given in Fig. 1. Specifically, a device with the following semi-optimized structural parameters and operational conditions: left barrier width of 2 nm, well width of 12 nm, right barrier width of 5 nm, Fermi level in emitter of 0.21 eV, Fermi level in collector of 0.099 eV, bias voltage of 0.093 V, and operating temperature of 280 K. The resulting CB resonant level E_2 and HH level E_1 are plotted together in Fig. 3. The figure clearly shows the transmission coefficient is a very good fit to the Breit–Wigner formula $|t_{Rc}|^2 = T_R \Gamma^2/[(E - E_{20})^2 + \Gamma^2]$, where E_{20} is the position of peak, T_R is the height of peak, and Γ is the half width of half maximum. In the example shown in Fig. 3, T_R is 0.61, E_{20} is 0.0386 eV, and Γ is 0.0014 eV. The resonant tunneling time is 0.47 ps from $\tau_{\mathrm{tr}} \sim \hbar/\Gamma$. The distance between the HH level E_h and E_{20} at $k_t = 0.05$ is 5.2 meV (238 μm, and 1.26 THz). The amplitude T_R and the position of E_{20} are found strongly dependent on k_t. As k_t increases, T_R decreases and E_{20} increases.
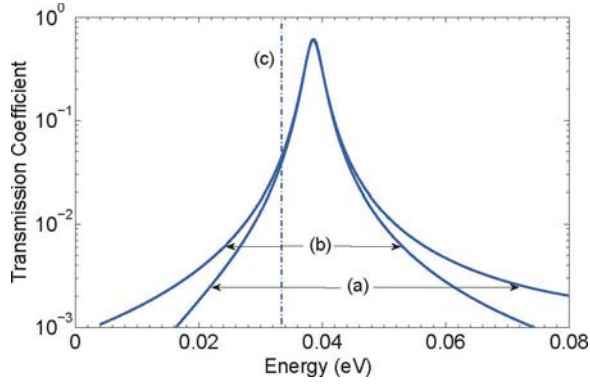
Fig. 3.   Conduction transmission coefficient at $k_t = 0.05$/nm. (a) Calculated results, (b) Fitting by Breit-Wigner's function, and (c) Position of heavy-hole level E_h relative the CB edge in the emitter.
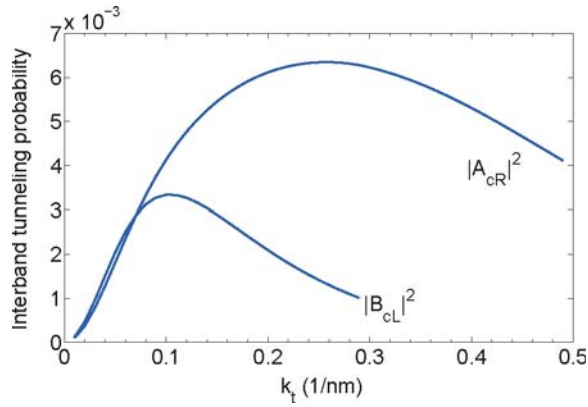

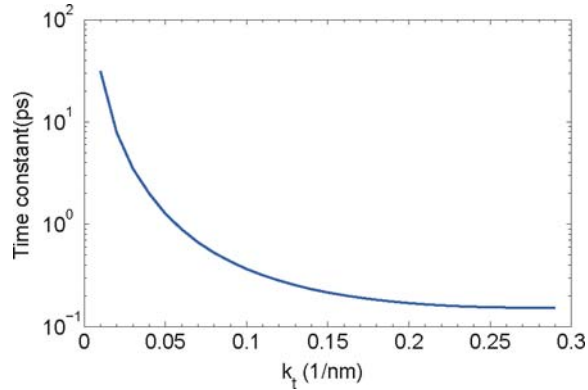Fig. 4.   Heavy-hole interband tunneling coefficients.

Fig. 5.   Heavy-hole interband tunneling time.

The tunneling probabilities $|A_{cR\pm}(k_t)|^2$ and $|B_{cL\pm}(k_t)|^2$ given in Fig. 4 demonstrate that HH interband tunneling is dependent on in-plane momentum. An important observation from Figs. 3 and 4 is that the interband tunneling probability is significantly less than the CB resonant-tunneling probability. The huge differences suggest the existence of two distinct electron transport pathes: CB resonant transport and HH interband tunneling. The small interband tunneling probability also justifies that the assumptions made in (12)–(14). Furthermore, the plot in Fig. 5 indicates right-hand side interband tunneling dominates over left-side interband tunneling (i.e., verifies that
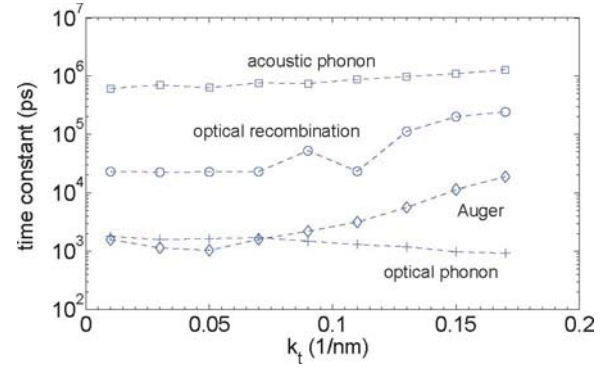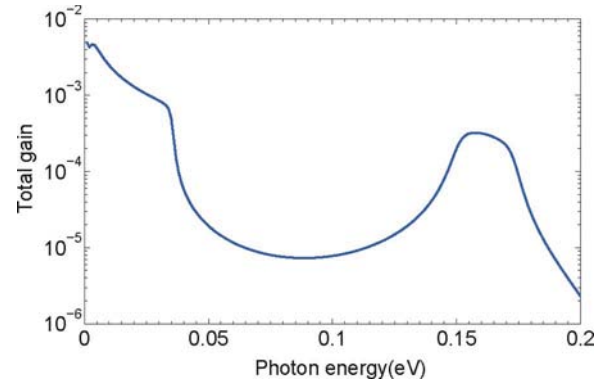

Fig. 6.   Transition rates.

Fig. 7.   Total gain at photon energy. The vertical axis is in log scale.

(23) is positive) when the active device region is tilted under bias voltage, so, HH hole accumulation occurs. In addition, the interband tunneling rate is always significant and only varying from on the order of 30 ps at $k_t = 0.01$/nm to as short as 0.4 ps at $k_t = 0.1$/nm.

All the relevant scattering processes and the optical recombination rate are plotted in Fig. 6 as a function of the particular final state (with momentum k_t). Here, one can observe that the optical phonon scattering lifetime is on the order of nanoseconds and the acoustic phonon scattering lifetime is on the order of hundreds of nanoseconds. Also, the Auger recombination lifetime is on the order of nanoseconds. These results sufficiently demonstrate that HH-interband tunneling is much faster than nonradiative processes, which is the key for the setup of stimulated emission. Furthermore, since the optical recombination is on the order of 20–100 ns, the interband tunneling is sufficient to maintain a population inversion.

The total gain G is plotted in Fig. 7. G is the integral of optical gain $g(z)$ over the active region which has the dimension of ~ 20 nm. Therefore, the optical gain $g(z)$ of this laser concept is significant ($\sim 10^3 \mathrm{cm}^{-1}$) in THz frequency range and shows promise for providing significant levels of output radiation of high spectral purity below 1 THz, where other proven laser concepts (e.g., quantum cascade) encounter difficulties. Hence, these preliminary research investigations offer a new avenue for the potential realization of a completely new type of THz solid-state laser. This envisioned THz laser has relevance to nanoscale science and technology because tools of this type

will be needed for the comprehensive analysis of nanoscale biological and/or organic systems that are well known to possess unique spectral signatures at very long wavelengths [15].

For practical laser operation, the CB-resonant tunneling injection should be minimized regarding issue of thermal dissipation. The operation current can be controlled in a tolerable range without significantly decreasing optical gain. For example, one can reduce the current by reducing the doping density (or the Fermi level) in emitter. Another possible approach to reduce injection current is to properly increase the thickness of left GaSb barrier.

III. Conclusion

This paper has provided physical models and numerical simulation results which support the premise that population inversions can be established between a CB-resonant tunneling-injection channel and a HH-interband depopulation channel that occur within InAs/GaSb broken-gap heterostructures and allow for radiative emissions at terahertz (THz) frequencies. Furthermore, a physical analysis based upon the application of the multiband Kane model for a particular InAs/GaSb broken-gap heterostructure laser design with semi-optimized structural and operational parameters suggests that significant optical gain can be obtained below 1 THz at high operating temperatures. Therefore, this novel interband resonant-tunneling device (I-RTD)-based laser concept has important relevance to the very long wavelength spectroscopic characterization of nanoscale biological and/or organic systems.

Acknowledgment

References

[1] H. Kroemer, "The 6.1 Å family (InAs, GaSb, AlSb) and its heterostuctures: A selective review," *Phys. E*, vol. 20, pp. 196–203, 2004.

[2] H. Ohno, L. Esaki, and E. E. Mendez, "Optoelectronic devices based on type II polytype tunnel heterostructures," *Appl. Phys. Lett.*, vol. 25, pp. 3153–3155, 1992.

[3] R. Q. Yang and J. M. Xu, "Population inversion though resonant interband tunneling," *Appl. Phys. Lett.*, vol. 59, pp. 181–182, 1991.

[4] R. Q. Yang, "Mid-infrared interband cascade lasers based on type-II heterostructures," *Microelectron. J.*, vol. 30, pp. 1043–1056, 1999.

[5] W. W. Bewley, C. F. Felix, I. Vurgaftman, D. W. Stokes, E. H. Aifer, L. J. Olafsen, J. R. Meyer, M. J. Yang, B. V. Shanabrook, H. Lee, R. U. Martinelli, and A. R. Sugg, "High-temperature continuous-wave 3-6.1 μm "W"Lasers with dismond-pressure-bond heat sinking," *Appl. Phys. Lett.*, vol. 74, pp. 1075–1077, 1999.

[6] B. Gelmont and D. Woolard, "Optical gain in an interband-resonant-tunneling-diode," in *Proc. 4th Conf. Nanotechnol.*, 2004, pp. 220–222.

[7] B. Gelmont, D. Woolard, and T. Globus, "Vertical-cavity laser based on interband-tunneling staggered-bandgap heterostructure," *Proc. SPIE*, vol. 6132, pp. 61320E1–61320E10, 2006.

[8] W.-D. Zhang and D. Woolard, "Far-infrared Terahertz basing based upon resoant and interband tunneling in InAs/GaSb heterostructure," *Appl. Phys. Lett.*, to be published.

[9] A. Yariv, *Quantum Electronics*, 3rd ed. New York: Wiley, 1988.

[10] B. Gelmont, D. Woolard, W.-D. Zhang, and T. Globus, "Electron transport within resonant tunneling diodes with staggered-bandgap heterostructures," *Solid State Electron.*, vol. 46, pp. 1513–1518, 2002.

[11] D. Woolard, W.-D. Zhang, and B. Gelmont, "A novel interband-resonant tunneling-diodes(I-RTD) based high frequency oscillator," *Solid-State Electron.*, vol. 49, pp. 257–266, 2005.

[12] S. L. Chuang, *Physics of Optoelectronic Devices*. New York: Wiley, 1995.

[13] P. J. Price, "Two-dimensional electron transport in semiconductor layers, I. phonon scattering," *Ann. Phys.*, vol. 133, pp. 217–239, 1981.

[14] C. Smith, R. A. Abram, and M. G. Burt, "Auger recombination in a quantum well heterostructure," *J. Phys. C: Solid State Phys.*, vol. 16, pp. L171–L175, 1983.

[15] D. L. Woolard, E. R. Brown, M. Pepper, and M. Kemp, "Terahertz frequency sensing and imaging: A time of reckoning future applications?" *Proc. IEEE*, vol. 93, no. 10, pp. 1722–1743, Oct. 2005.

Weidong Zhang (S'03–M'05) received the Ph.D degree in engineering physics from the University of Virginia, Charlottesville, in 2005, where he studied device physics.

He is currently in the Department of Electrical and Computer Engineering, North Carolina State University, Raleigh. His research interest includes electronic devices for submillimeter/terahertz applications.

Dwight L. Woolard (F'04) received the Ph.D. degree from North Carolina State University, Raleigh, in 1991.

Since 1993, he has been with the U.S. Army Research Laboratory (ARL), U.S. Army Research Office, Research Triangle Park, NC, where he is currently the Leader of one of the largest U.S. research programs in terahertz-frequency science and technology, and manages the research program on solid-state and high-frequency electronics, which emphasizes terahertz-frequency and ultrafast electronics, nanoelectronics engineering science, and advanced solid-state device concepts. He has pioneered the development of terahertz spectroscopy for biological-agent sensing. His research interests include terahertz-frequency biosensing and terahertz-frequency oscillations in solid-state tunneling devices.